Manuscript LaTeX file
Click here to download Manuscript: pfreeman_CEP.tex
Click here to view linked References

Air data system fault modeling and detection

P. Freeman[a,1,*], P. Seiler[a,2], G.J. Balas[a,3]

[a]*Department of Aerospace Engineering and Mechanics, University of Minnesota, 107 Akerman Hall, 110 Union Street SE, Minneapolis, Minnesota 55455, United States*

Abstract

Air data probes collect essential measurements of aircraft airspeed, altitude, and attitude, and erroneous measurements jeopardize an aircraft and its passengers. To mitigate erroneous measurements, sensor hardware redundancy is typically combined with a voting system. Redundancy, however, may result in unacceptable increases in system weight and cost. This paper investigates a model-based alternative to hardware redundancy which requires an accurate mathematical representation of faulted and unfaulted air data probes. This paper models the most common air data probe fault modes–blockages due to debris, ice, or water–using physical air data relationships and experimental wind tunnel data. These models are used to design robust, model-based fault detection filters for the NASA GTM aircraft. Two linear H_∞ filters are synthesized to detect faults, reject exogenous disturbances, and provide robustness to model errors. The filters are designed using linearized aircraft models at one flight condition. Detection performance

*Corresponding author
Email addresses: freeman@aem.umn.edu (P. Freeman), seiler@aem.umn.edu (P. Seiler), balas@aem.umn.edu (G.J. Balas)
[1]Graduate Student, University of Minnesota
[2]Assistant Professor, University of Minnesota
[3]Professor, University of Minnesota

is evaluated using experimentally-derived fault models with the nonlinear aircraft simulations in the presence of actuator uncertainty.
Keywords: aerospace engineering, air data systems, fault detection, fault tolerance, pressure measurements, robust estimation, sensor failures

---

1. Introduction

New methods of system monitoring, fault detection, and fault diagnosis can enhance the safety and reliability of increasingly advanced technological systems. These performance demands are particularly important for systems in which a malfunction can result in significant equipment damage, costly environmental harms, injuries, or deaths. These systems, known as *safety-critical* or *life-critical* systems, require the highest resilience to malfunction that engineers can achieve. Such processes are traditionally found in energy infrastructure, medical devices, transportation, and weapons systems.

The unique operational missions associated with each platform engender different responses to system failure. The development of fault-tolerant systems is of increasing interest within a multitude of fields. Fault-tolerance is one approach for avoiding operational failures when faults occur. The system may operate safely despite the presence of a fault by executing a reconfigured control strategy. Detection and isolation of faults are key components for fault-tolerant systems.

Stringent safety requirements have driven aircraft system design for decades. The system availability and integrity requirements for commercial flight control electronics are typically no more than 10^{-9} catastrophic failures per flight hour (Bleeg, 1988; Collinson, 2003). The typical industry design solution is

based extensively on physical redundancy at all levels of the design. For example, the Boeing 777 has 14 spoilers, 2 outboard ailerons, 2 flaperons, 2 elevators, one rudder and leading/trailing edge flaps (Yeh, 1996, 1998). Each of these surfaces is driven by two or more actuators, all connected to different hydraulic systems. The inertial and air data sensors have a similar level of redundancy and are critical for flight safety.

1.1. Historical Failures due to Air Data Faults

Air data sensor suites provide a variety of critical measurements for the aircraft control systems and pilots. Total and static pressure measurements–combined with total air temperature–are used to compute altitude, vertical speed, and airspeed. Angle of attack and sideslip sensors provide measurements of the aircraft orientation relative to its net velocity vector. Aircraft dynamics can vary significantly when flying at different attitudes, airspeeds, and altitudes, and accurate air data measurements allow for proper aircraft operation. Erroneous measurements, however, can induce dangerous maneuvers with sometimes catastrophic consequences. Thus, the integrity and reliability of air data is paramount for safe flight.

This paper focuses on characterization of faults affecting air data pressure sensors. A typical commercial aircraft employs three pitot-static probes, such as those shown in Figure 1, to determine airspeed and altitude. The probes have ports (holes) at the tip to capture and stagnate air in order to measure total pressure. Static pressure ports are on the sides of the probes, oriented perpendicular to the airflow. The static and total pressure channels exit at the bottom of the probe and connect to pressure transducers. These probes are mounted on the fuselage, pointing into the airflow, and are typically

placed near the nose of the aircraft.

Failures of these probes have resulted in numerous fatal accidents of commercial, military, and general aviation aircraft. To address these failures, sensor hardware redundancy is typically combined with voting systems to detect and discard erroneous measurements. The redundancy-dependant control architectures, e.g. multiple air data systems, used in the aircraft industry achieve extraordinarily high levels of availability and integrity, yet catastrophic failures do occur. Two recent examples of notable air data system failures are:

Figure 1: Examples of pitot-static probes

- B-2 Spirit bomber crash – 2008 In February 2008, a USAF B-2 Spirit bomber collected erroneous air data measurements that led to a crash and total loss of the $1.4 Billion aircraft in Guam (ACC News Service, 2008). According to investigators, moisture in the aircraft's pressure transducer units during air data calibration distorted the information

in the bomber's air data system, causing the flight control computers to calculate an inaccurate airspeed and a negative angle of attack upon takeoff. This led to an, "uncommanded 30 degree nose-high pitch-up on takeoff, causing the aircraft to stall and its subsequent crash."

- Air France/Airbus A330 Flight 447 crash – 2009 In June 2009, Air France Flight 447 plummeted over 11 km in only 3.5 minutes and crashed mysteriously over the Atlantic Ocean en route to Paris (Bureau d'Enquêtes et d'Analyses, 2011). The flight data recorders were recovered after a nearly two-year hunt. The recovered data appeared to indicate that the pilots had conflicting air speed data in the minutes leading up to the crash. The aircraft climbed to 11.5 km when "the stall warning was triggered and the airplane stalled," according to the investigators' report. Investigators suspect that the aircraft's pitot probes malfunctioned due to ice at high altitude.

1.2. Motivation for Model-based Analytical Redundancy

The use of physical redundancy dramatically increases system size, complexity, weight, and power consumption. Moreover, design, development, and unit production of such systems is expensive. There is an increasing demand for high-integrity, yet low cost, fault tolerant aerospace systems (e.g. unmanned aerial vehicles and fly-by-wire capabilites) in lower-end business and general aviation aircraft. Supplanting physical redundancy with analytical redundancy that still maintains reliability can reduce costs and facilitate the development of such vehicles.

If a sufficiently accurate model of the system is available, model-based methods can be used to estimate system states and outputs. Model-based

redundancy approaches rely upon an accurate mathematical model of the underlying physical relationships present within a system. By representing common fault modes in this manner, simulations of fault manifestations are performed and a fault detection scheme can be constructed.

The fault detection problem usually comprises a method to compute residuals and a process to declare faults based on the residuals. It is desired that the generated residual be a good representation of the fault of interest while being insensitive to process and measurement noises. Generation of residuals depends on the information available about the system. A keen understanding of faulted system performance from an accurate mathematical model can be used to optimize performance of a fault detection filter to meet particular specifications that other approaches may be ill-suited to meet. See (Gertler, 1998; Isermann, 2005; Ding, 2008b) for a detailed treatment of model based and model-free fault detection methods.

This paper focuses on the development of accurate fault models and model-based fault detection and isolation for air data systems. The air data probe fault models are derived from experimental wind tunnel tests performed at a variety of flight conditions. The H_∞ model-based framework is used to design an analytical fault detection filter for an air data system.

1.3. Outline

This paper has the following structure: Section 2 describes the basic air data relationships, pitot-static probe operation, and common faults affecting these probes. Mathematical blockage fault models of the air data systems are derived from first principles and experimental tests. An aircraft platform is chosen for study, and models for the aircraft, controls, and additional sensor

systems are discussed in Section 3. Section 4 describes the H_∞ methods used to design two robust fault detection filters. Fault detection simulation results and analysis for four blockage fault modes are given in Section 5. Finally, Section 6 discusses conclusions and directions for future research.

2. Air Data Sensors

This section describes the physical relationships used to create air data measurements, the structure and operation of a typical pitot-static air data probe, common fault modes, and experimental data associated with individual fault conditions. This information is used to construct fault models that are important to the development of fault detection algorithms.

2.1. Air Data Relationships

The basic relationships between air data measurements and aircraft states are derived in (Collinson, 2003). For altitudes in the troposphere (up to $\approx$ 11 km), the static pressure p_s is related to altitude h by:

$$h = \frac{T_0}{L}\left(1 - \left(\frac{p_s}{p_{s_0}}\right)^{LR/g}\right) \tag{1}$$

where $T_0 := 288.15K$ is the absolute temperature at sea level, $L := 6.49\frac{K}{km}$ is the troposphere lapse rate, $g := 9.81\frac{m}{s^2}$ is the standard gravity at sea level, $p_{s_0} := 101.325kPa$ is the static pressure at sea level, and $R := 287\frac{J}{kg \cdot K}$ is the specific gas constant for dry air.

For compressible air and subsonic speeds, the static and total (pitot) pressures, p_s and p_t, are related to the calibrated (indicated) airspeed V_c

(m/s) by:

$$V_c = A_0 \sqrt{5 \left(\frac{p_t - p_s}{p_{s_0}} + 1 \right)^{2/7} - 5}; \tag{2}$$

where $A_0 := 340.29$ m/s is the speed of sound at sea level. The calibrated airspeed is equal to the true airspeed at sea level but the two airspeeds differ at altitudes above sea level. A more accurate model at high altitudes would include a model of the total air temperature sensor used to compute true airspeed (Goodrich, 2002). The more simplistic air data model, Equations 1 and 2, is used in this paper; hence, the air data models are only valid at low altitudes. The flight regime considered in this paper is restricted to low altitudes less than 1 km. Thus, Equations 1 and 2 provide a sufficiently accurate model for such analysis.

2.2. Pitot-Static Probe Operation

A fully operational pitot-static probe, as shown in Figure 2, measures static pressure, p_s and total pressure, p_t, using independent pressure lines and transducers. The probe captures freestream airflow via the pitot inlet port, and the moving air stagnates within the channels inside the probe. The total pressure is measured at the pitot pressure output. A static pressure measurement is obtained via small-diameter static ports that are flush with the fuselage of the probe. Static pressure is measured by a pressure transducer at the static pressure output. Dynamic pressure, $p_{dyn} = p_t - p_s$, is a calculated quantity (Collinson, 2003; Goodrich, 2002).

Air entering the probe can contain significant moisture. This moisture must be removed from the probe in order to prevent excessive accumulation of water that can lead to blockage faults. In a fully-operational probe, gravity

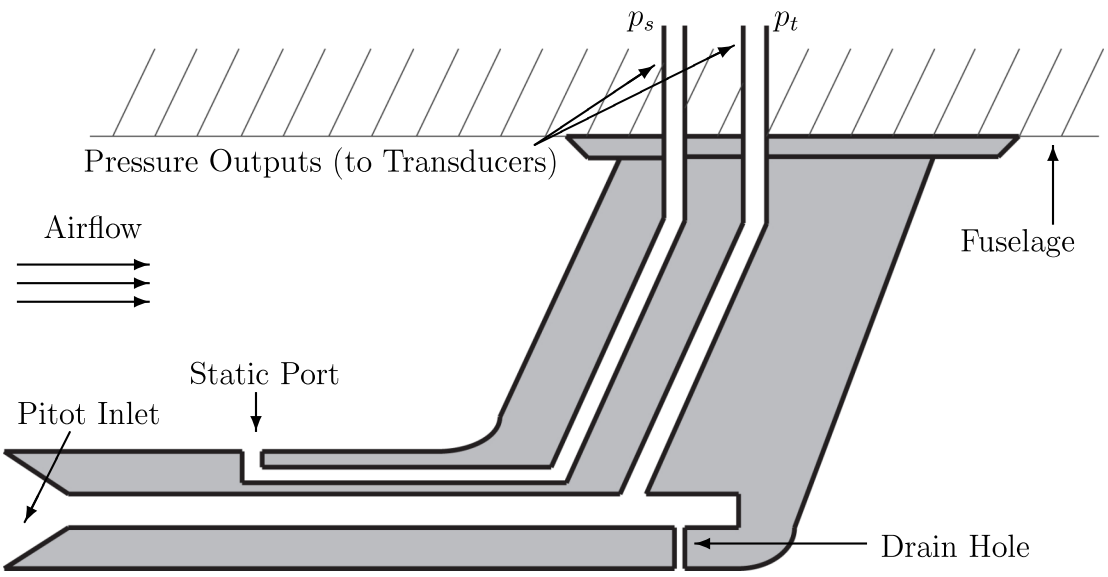

Figure 2: Pitot-static probe

moves water inside the probe to a small drain hole. The pressure differential between the pitot inlet (total pressure) and drain hole (static pressure) forces water out of the the drain hole. This hole is quite small in comparison to the pitot opening, hence there is minimal pressure loss at the pitot pressure output due to the drain hole.

2.3. Industry Standards

The accuracy specifications of air data systems are driven primarily by vehicle operational requirements. Commercial and general aviation aircraft are subject to Federal Aviation Administration (FAA) regulations in the United States and European Aviation Safety Agency (EASA) regulations in the European Union.

Certification for Reduced Vertical Separation Minima (RVSM) compliance requires particular avionics systems that each have their own specifica-

tions. EASA requires airplanes operated in RVSM airspace to be equipped with:

1. Two independent altitude measurement systems;
2. An altitude alerting system;
3. An automatic altitude control system; and
4. A secondary surveillance radar (SSR) transponder with altitude reporting system that can be connected to the altitude measurement system in use for altitude keeping.

The United States maintains similar standards (Federal Aviation Administration, 2009). To ensure that aircraft can safely operate in close proximity, the maximum allowable altimetry system error is 245 feet (approx. 75 m). Thus, based on Equation 1, a static pressure fault as large as $\pm$ 0.1 psi (.069 kPa) would lead to an altitude error of nearly 200 feet (over 60 m), close to the maximum error allowed for an air data system. These standards provide insight into the significance of pressure errors of a given size; the fault detection algorithms in this paper are tested against realistically severe air data system faults.

2.4. Fault Modes and Modeling

This section details common fault modes for pitot-static probes, their potential causes, and their effects on air data measurements. There are three broad classifications of faults affecting in air data probes: blockage faults, airflow disruption faults, and heater-related faults. Some faults induce the same qualitative measurement errors across all flight conditions, while other

faults will manifest themselves differently depending upon aircraft maneuvering. This paper primarily examines common blockage fault modes, and models of those fault modes are used for fault detection filter synthesis and simulation. A description of the different fault modes and their manifestations in air data follows. Other fault modes, such as airflow disruption faults and heater-related faults require advanced modeling beyond the focus of this paper, yet remain relevant problems in the aerospace industry. A brief overview of the effects and challenges associated with these faults is also provided.

Blockage Faults

Pitot-static probes are exposed to the elements making them vulnerable to blockage faults. The impact of blockage faults on the aircraft depends on the location of the blockage(s) and the aircraft maneuvers. Pneumatic lines within the probes transmit the static and total pressures to pressure transducers. Faults in the pneumatic lines can significantly alter air data measurements.

Blockage faults can occur as a result of a variety of causes:

- Exterior Icing (unpowered heater, failed heater, conditions exceed anti-icing capabilities)
- Water or ice accumulation in pressure line
- Insects (e.g. Mud Dauber Wasp)
- Bird Strike
- Debris

- Protective cover left in place

An overview of common blockage faults is now provided.

Drain Hole Blockage. With a blocked drain hole and an open pitot inlet (Figure 3), the air data measurements will be slightly erroneous. The air data transducers are calibrated to account for the pitot pressure losses that occur with a nominally-performing (i.e. open) drain hole. In the event that the hole experiences a blockage, the calibration induces a small error, i.e. a small false increase in airspeed. Moreover, and perhaps more seriously, the probe has a high probability of collecting water which can enter the pressure lines and corrupt measurements. The static pressure measurement, and hence the altitude measurement, will be unaffected by a drain hole blockage.

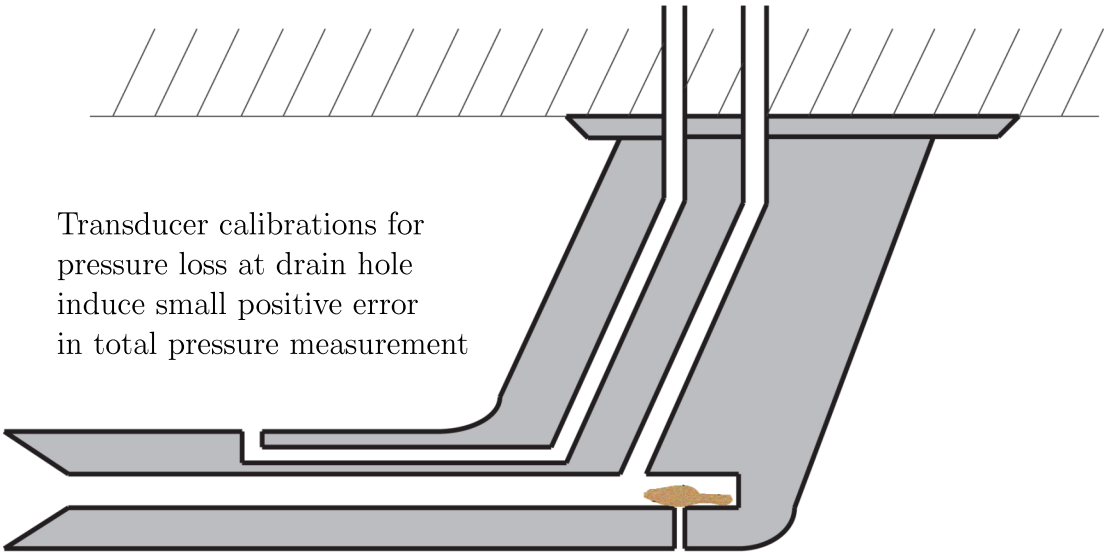

Figure 3: Pitot-static probe with drain hole blockage

A pitot-static probe with a blocked drain hole was tested in a subsonic

wind tunnel on an airspeed versus angle-of-attack grid to simulate fault effects at varying flight conditions. Tests were performed on an evenly-spaced grid of 25 to 200 knots airspeed and -15 to 15 degrees angle of attack. The pressure data was measured at 25 knot and 5 degree increments.

The air pressure measurements were examined in nondimensional form; the error between the test probe measurement p_{probe} and a calibrated tunnel reference probe measurement p_{ref} is nondimensionalized by the tunnel dynamic pressure q_c as shown in Equation 3. Note that the tunnel dynamic pressure measurement is gathered by the tunnel reference probe, not the test probe.

$$p_{s_{ND}} = \frac{(p_{s_{probe}} - p_{s_{ref}})}{q_c}; \quad p_{t_{ND}} = \frac{(p_{t_{probe}} - p_{t_{ref}})}{q_c} \tag{3}$$

Nondimensionalizing in this way allows for an understanding of the quality of a set of air data measurements that spans a broad flight regime.

These wind tunnel experimentations allow for comparisons of nominal and faulted static and total pressure measurements across airspeed sweeps for each angle of attack. The residuals, or errors, associated with this fault mode are shown in Figures 4. The mean errors for this fault mode over the entire airspeed sweep is shown for each angle of attack in Figure 5. Based on the experimental results in figures 4-5, it is clear that a drain hole blockage has little to no impact on the static pressure measurement indicated by the probe. This is true across different airspeeds and angles of attack. At negative angles of attack, however, the geometry of the probe is such that the static port captures a component of the dynamic pressure; this is reflected in elevated static pressure indicated by the probe relative to the tunnel reference static pressure. This effect diminishes as the angle of attack increases, and for $\alpha \geq$

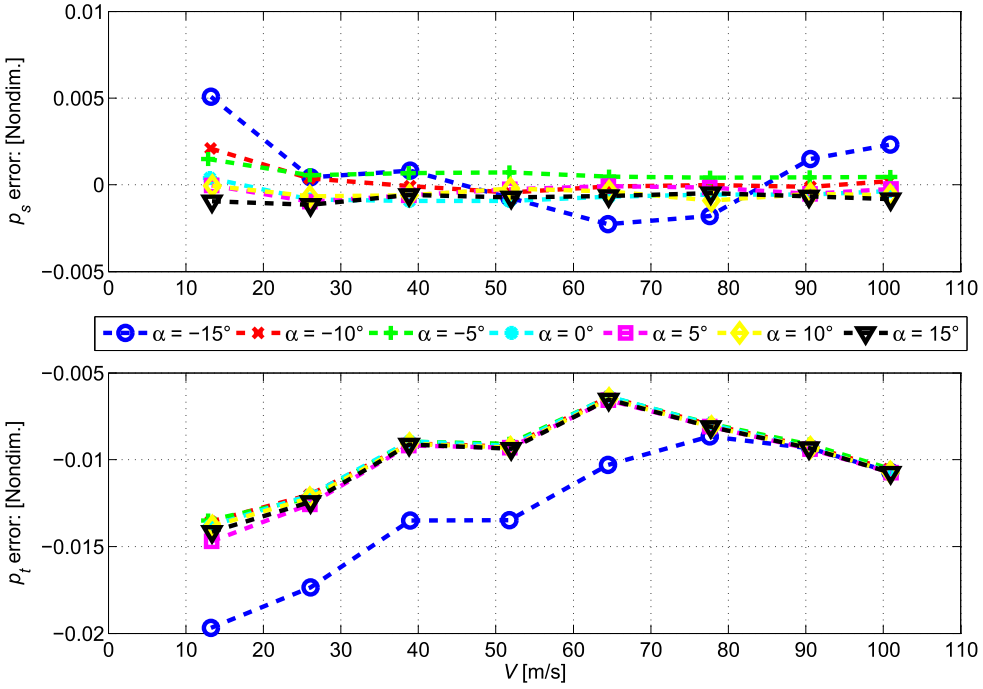

Figure 4: Air data measurement errors for a drain hole blockage.

0, this behavior is no longer evident in the experimental results. The effect of angle of attack upon the total pressure measurement error is less significant than the small effect it has upon the static pressure measurement error. Thus, in most flight scenarios, angle of attack is not an important predictor of drain hole blockage effects. The airspeed at which the total pressure measurement error magnitude is minimized is approximately 65 m/s, and the error magnitude begins increasing again as airspeeds increase. A commercial airliner would easily exceed the airspeeds examined in these experiments, however for the vehicle platform considered in this research (described in the following chapter), these airspeeds are appropriate.

The drain hole blockage experimental results also indicate that there is

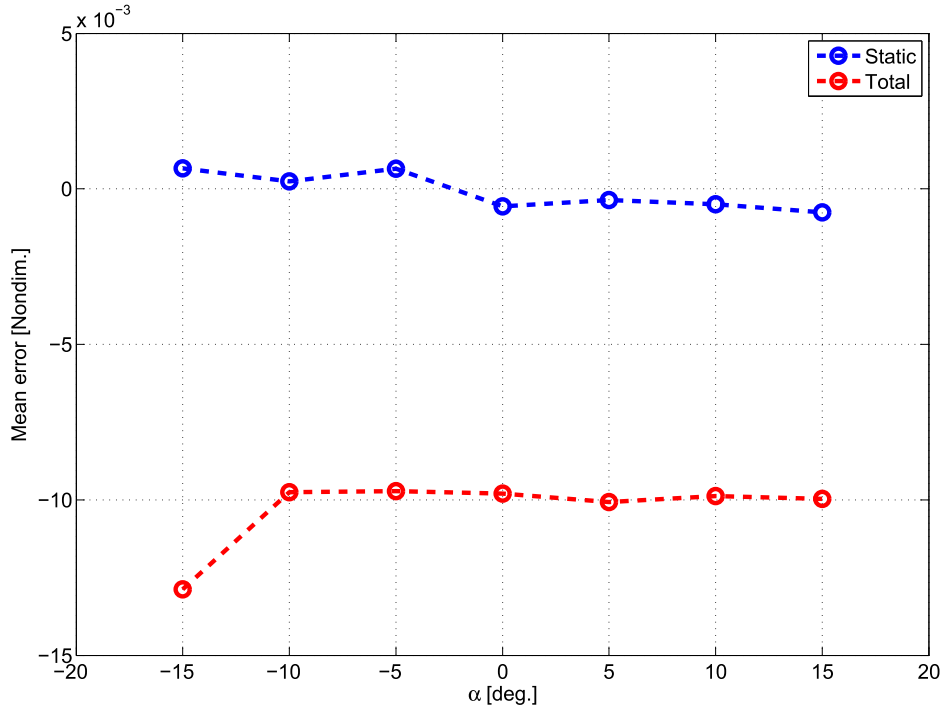

Figure 5: Mean errors at each angle of attack for airspeed sweeps.

a small false increase in the total pressure measured by the faulted probe. Since the static pressure measurement in a faulted probes remains nearly correct, the increase in the total pressure measurement would erroneously indicate an increased airspeed. The overall effect of this fault, as evidenced by Figure 5, is consistent throughout the envelope tested. The fault magnitude is exacerbated, however, for large magnitude, negative angles of attack due to the geometry of tested probe. These results provide some insight into the effects of drain hole blockages, but specific probes can be more or less impacted by faults depending on the probe design. For this particular fault mode, the pressure measurements can be thought of as an additive positive step on the true value of the total pressure *only*. The air data system should

record static pressure values that are accurate. This indicates that selective step faults are strong candidates for simulating this real fault scenario.

It should also be noted that for drain hole blockages – as well as other blockage faults – partial blockages can induce similar effects upon the air data measurements as the corresponding full-blockage fault.

Pitot Inlet Blockage. A blocked pitot inlet and an open drain hole (Figure 6) result in the drain hole becoming a static port. Hence, the total pressure output will match the static pressure output. A pitot inlet blockage, however, is not evident at the beginning of a takeoff roll because the pilots and aircraft avionics are not anticipating a dynamic pressure indicative of a moving aircraft.

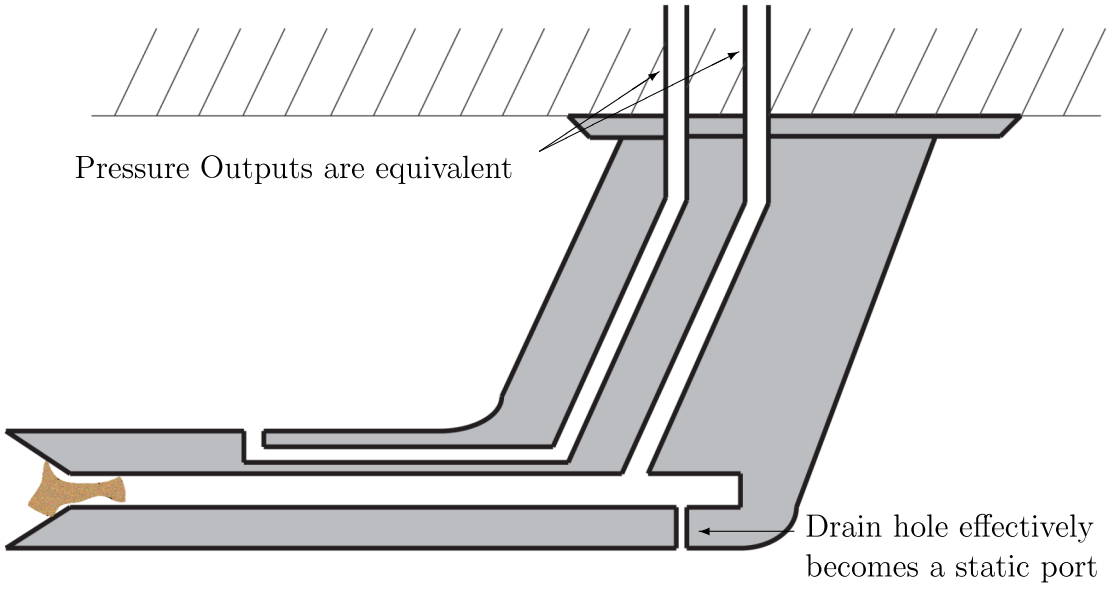

Figure 6: Pitot-static probe with pitot inlet blockage

Pitot Inlet and Drain Hole Blockages. A pitot inlet blockage combined with a drain hole blockage (Figure 7), presents a more complex set of effects. In this case, the pitot pressure channel becomes a closed system, and the pressure therefore remains constant during all aircraft maneuvers. The indicated airspeed will be misleading in a variety of ways depending upon the particular aircraft maneuver.

When the aircraft climbs with both the pitot inlet and drain hole blocked, the static pressure correctly decreases while the dynamic pressure incorrectly increases. In a descent, the static pressure correctly increases while the dynamic pressure incorrectly decreases. For an aircraft increasing or decreasing in airspeed, the dynamic pressure incorrectly remains constant. Table 1 describes the effects of a drain hole blockage combined with a pitot inlet blockage on the airspeed and altitude measurements.

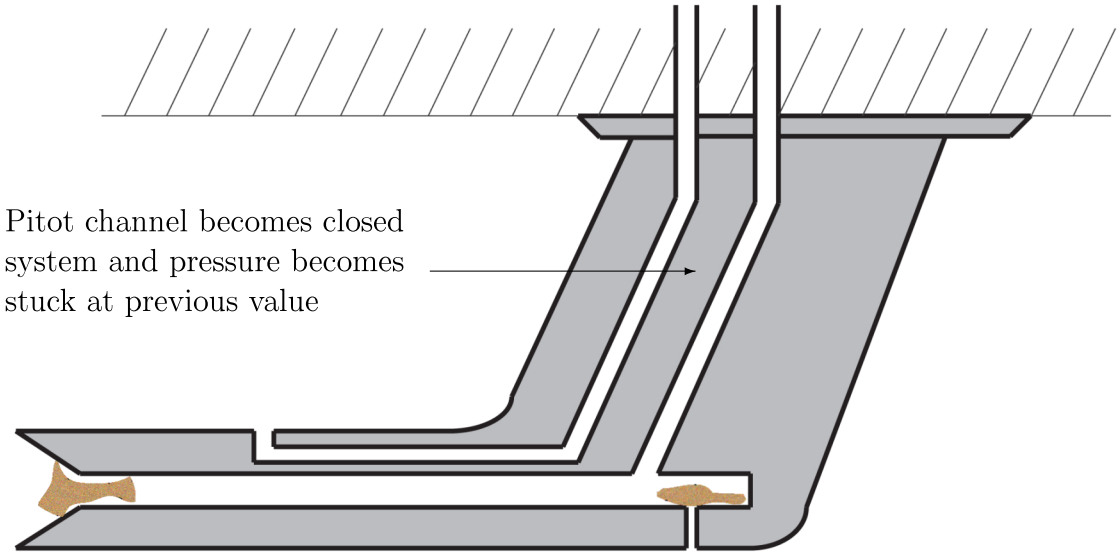

Figure 7: Pitot-static probe with combined pitot inlet and drain hole Blockage

Table 1: Blockage fault effects for pitot-static probes

Blockage	**Maneuver**	V **Measurement**	h **Measurement**	**Figure**
Drain	All	False increase	Correct	Fig. 3
Pitot Inlet	All	Stuck at zero	Correct	Fig. 6
Drain and Pitot Inlet	Climb	False increase	Correct	Fig. 7
	Descent	False decrease	Correct	
	Increasing V	Falsely constant	Correct	
	Decreasing V	Falsely constant	Correct	
Static Port	Climb	False decrease	Falsely constant; altitude rate stuck at zero	Fig. 8
	Descent	False increase		
	Increasing V	Correct		
	Decreasing V	Correct		
Water in Probe	All	Various	Various	Fig. 9

Static Port Blockage. A blocked static port (Figure 8) directly impacts the altitude measurement and adversely impacts the dynamic pressure (and thus indicated airspeed) in a manner similar to a pitot inlet blockage. When the aircraft climbs, the static pressure incorrectly remains constant while the dynamic pressure incorrectly decreases. In a descent, the static pressure incorrectly remains constant while the dynamic pressure incorrectly increases. When increasing or decreasing in airspeed while maintaining a particular altitude, the static and dynamic pressure are correct. Table 1 describes the effects of a static port blockage on the airspeed and altitude measurements.

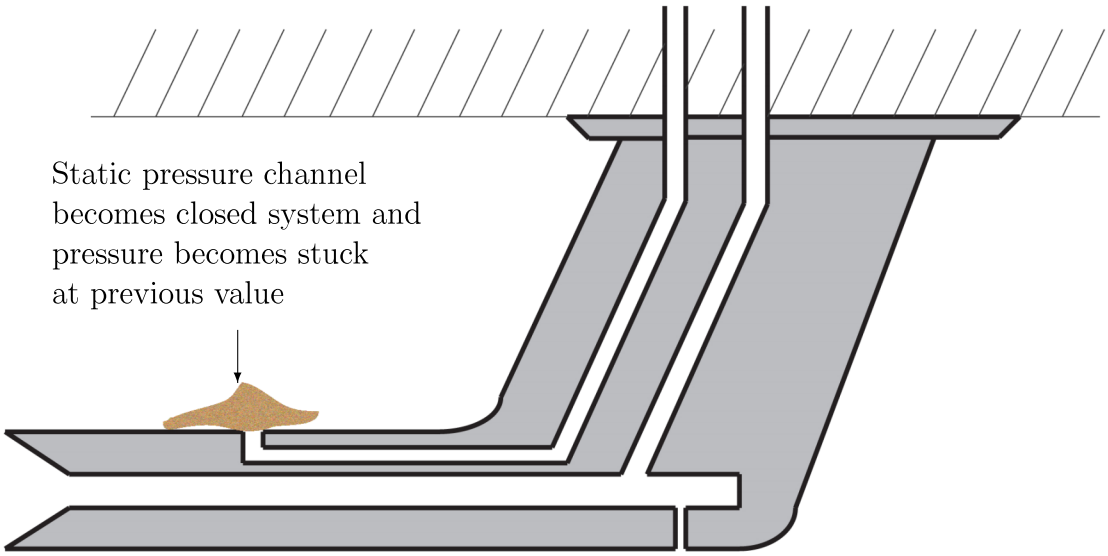

Figure 8: Pitot-static probe with static port blockage

Water in Probe or Pressure Lines. The presence of water within an air data probe or its attached pressure lines (Figure **??**) can lead to significant fluctuations in pressure measurements. A meniscus formed within a pressure line will cause increased pneumatic lag due to the weight of the water present in the line. The magnitude of the pressure fluctuations and the associated pneumatic lag is influenced by the mass and location of the water in the line. Unlike with port blockages, the potential effects of this fault on the altitude and airspeed measurements are not as clearly defined.

A summary of blockage fault effects is presented in Table 1. When a fault does not impact the validity of a particular measurement, the corresponding table entry indicates that the measurement is 'Correct.' Aircraft maneuvers mentioned in Table 1 are assumed to be independent (i.e., a change in airspeed occurs while the aircraft maintains constant altitude, and vice versa).

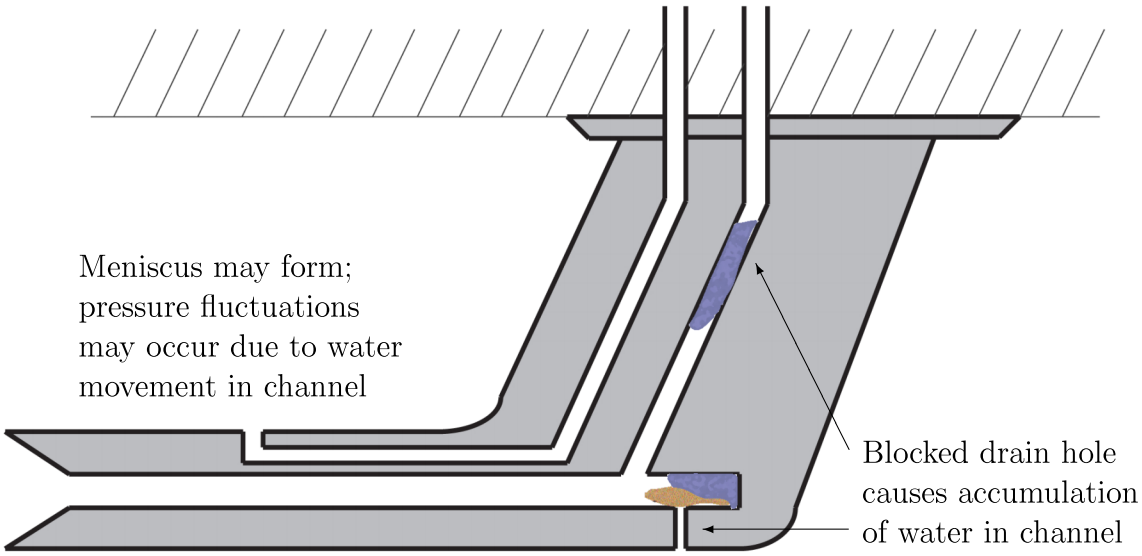

Figure 9: Pitot-static probe with water blockages

Pneumatic Line Leakage. Air pressure is conveyed to the pressure transducers via pneumatic lines attached to the air data probe. Leakages in the pneumatic lines corrupt pressure measurements. The particular effects of such a fault depend upon which system is leaking (pitot or static), leakage severity, and the ambient pressure in the location of the leak. Leaks could occur in a pressurized cabin compartment or in an unpressurized bay; the ambient pressure in the location of the leak influences the magnitude and direction of any errors in the air data measurements.

Airflow Disruption Faults

Pitot-static probes are placed in locations on an aircraft fuselage which are expected to experience laminar airflow that is unlikely to be fouled in-flight by moving control surfaces or by the fuselage itself. While this provides

for maximum sensor accuracy, airflow disruptions that do occur may still adversely impact measurements collected by the air data probes. The most common example of such airflow disruptions can occur with aircraft icing. Icing-related blockage faults internal to pitot-static probes were previously discussed; ice accretion on the fuselage or the exterior of the probe can significantly disrupt airflow in the vicinity of the static ports. Depending on the flow disruption, the measured static pressure could be greater or smaller than the actual static pressure. In such a case, provided that the a clean airflow is available for the pitot inlet, the pitot pressure measurement is unlikely to be significantly impacted.

Heater Faults

Pitot-static probes contain heaters embedded within their surfaces which discourage ice accretion on the surface of the probe and melt ice crystals which may have entered the pitot inlet, allowing for proper drainage and preventing blockages. Heater elements can completely fail (in which they short circuit and no longer provide any heat) or experience slow-acting faults such as resistance drift. Changing resistances of the heater element cause fluctuations in heat output. Abnormal heating fluctuations can cause varying temperatures in the air volumes in the pneumatic lines and can affect the pressure measurements. Unlike blockage faults, heater faults can manifest themselves more slowly, and often gradually, since internal probe temperatures will not change abruptly. When ice accretion occurs on the probe and/or fuselage due to heater failure, however, air data systems additionally become susceptible to blockage and airflow disruption faults.

Faults Studied and Future Modeling Work

The focus of this paper is full and partial blockage fault detection. Blockage faults tend to be fast-acting and cannot necessarily be predicted via regular monitoring and maintenance (although consistent probe cleaning minimizes risk). Blockage faults also tend to lead to either 'stuck-at' values for pressure measurements or a bias in the measurement that is largely unchanged at a given flight condition. This behavior makes blockage faults easier to model and simulate. There are instances, however, where a partial blockage or the presence of water in the pressure lines could lead to time-varying adverse effects on the air data measurements. Faults relating to airflow disruptions (e.g. from icing) or heater faults involve more complex studies of icing aerodynamics and heater element construction and control. In order to investigate fault-tolerance approaches for these failure scenarios, higher fidelity models of the air data probes are necessary. Extensive consideration of these fault modes is beyond the scope of this paper, but heater and airflow disruption effects are strong candidates for future model development.

Blockage faults in the air data system will be modeled as additive step changes in the static pressure measurement, total pressure measurement, and both measurements simultaneously in the subsequent section. Additionally, time-varying effects from water blockages or other fault scenarios will be modeled as additive sinusoidal changes in the pressure measurements. These models will be integrated into a high fidelity 6 degree-of-freedom simulation model of a subscale commercial aircraft testbed for performance evaluation.

Pressure Measurement Processor Model

The pressure transducers are modeled by inverting the functions in Equations 1-2 to obtain values of static and total pressure from the aircraft altitude and airspeed. This yields the expected values for the pressures based upon the aircraft state assuming a standard atmosphere model. To model sensor noise and faults in the pressure measurements, the nominal pressure signals are corrupted by white noise and faults are added to the pressure signals to yield pressure measurements.

Pressure transducer measurements are processed onboard the aircraft to yield derived altitude and airspeed measurements for feedback to the control loops and to the pilot. Equations 1-2 are applied in the simulation to produce altitude and airspeed measurements from pressure measurements. In this paper, all pressure signals have units of kPa. The air data system architecture model is depicted in Figure 10.

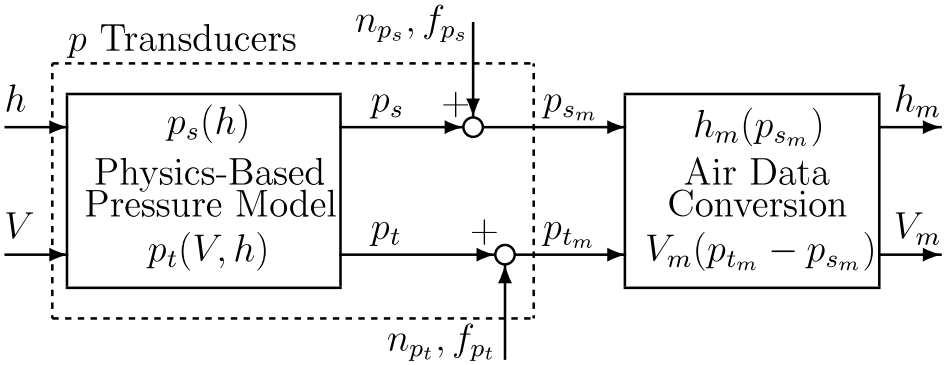

Figure 10: Air data sensor architecture

The aircraft test bed to be described in the subsequent section operates at low airspeeds and low altitudes. Choosing a flight condition within the aircraft flight envelope and linearizing the air data conversion equations about

that state reveals insight into appropriate magnitudes for injected faults. Equation 4 shows linearized air data model at 38.5 m/s airspeed and 152 m altitude.

$$\begin{bmatrix} \delta h_m \\ \delta V_m \end{bmatrix} = \begin{bmatrix} -4016 & 0 \\ -3771 & 3771 \end{bmatrix} \begin{bmatrix} \delta p_s \\ \delta p_t \end{bmatrix} \tag{4}$$

From Equation 4, a fault (error) of magnitude .069 kPa (0.01 psi) in p_s would yield an h_m error of -5.82 m and -1.45 m/s in V_m. A fault of the same size in p_t will result in a V_m error of 1.45 m/s. Equation 4 shows that faults injected on p_s and p_t both influence V_m. If the faults are simultaneous in both p_s and p_t and of equal magnitude and sign, V_m will be unaffected.

3. Aircraft Model

This section describes the aircraft model used as a platform for fault detection filter design and simulation. The platform considered for this research is the NASA Generic Transport Model (GTM), a remote-controlled, 5.5 percent dynamically-scaled commercial aircraft (Murch & Foster, 2007). The aircraft weighs approximately 25 kg and can reach airspeeds of up to 90 m/s. A high fidelity 6 degree-of-freedom nonlinear model of the GTM (Cox, 2010) was developed by NASA with the aerodynamic coefficients provided as look-up tables. The nonlinear simulation captures key flight dynamics characteristics of the GTM aircraft and the commercial transport aircraft after which it is designed and provides a useful starting point for this analysis.

3.1. Generic Transport Model Longitudinal Dynamics

This section describes the longitudinal dynamics of the GTM aircraft. GTM aircraft geometric and mass parameters – as well as relevant constants –

are provided in Table 2. The longitudinal dynamics of the GTM are described

Table 2: Aircraft and environment parameters

Parameter	**Value**
Wing Area, S	0.548 m^2
Mean Aerodynamic Chord, $\bar{c}$	0.279 m
Mass, m	26.2 kg
Pitch Axis Moment of Inertia, I_{yy}	6.311 kg-m^2
Air Density, ρ	1.225 kg/m^3
Gravity Constant, g	9.807 m/s^2

by a standard five-state longitudinal model (Stevens & Lewis, 1992):

$$\dot{V} = \frac{1}{m}\left(-D - mg\sin\left(\theta - \alpha\right) + T_x\cos\alpha + T_z\sin\alpha\right) \tag{5}$$

$$\dot{\alpha} = \frac{1}{mV}\left(-L + mg\cos\left(\theta - \alpha\right) - T_x\sin\alpha + T_z\cos\alpha\right) + q \tag{6}$$

$$\dot{q} = \frac{\left(M + T_m\right)}{I_{yy}} \tag{7}$$

$$\dot{\theta} = q \tag{8}$$

$$\dot{h} = V\sin(\theta - \alpha) \tag{9}$$

where V is air speed (m/s), α is angle of attack (deg), q is pitch rate (deg/s), θ is pitch angle (deg), and h is altitude (m). The control inputs are the elevator deflection δ_{elev} (deg) and engine throttle δ_{th} (percent).

The drag force D (N), lift force L (N), and aerodynamic pitching moment

M (N-m) are given by:

$$D = \bar{p}SC_D(\alpha, \delta_{elev}, \hat{q}) \tag{10}$$

$$L = \bar{q}SC_L(\alpha, \delta_{elev}, \hat{q}) \tag{11}$$

$$M = \bar{q}S\bar{c}C_m(\alpha, \delta_{elev}, \hat{q}) \tag{12}$$

where $\bar{q} := \frac{1}{2}\rho V^2$ is the actual (not a measured quantity, unlike p_dyn) freestream dynamic pressure (kPa) and $\hat{q} := \frac{\bar{c}}{2V}q$ is the normalized pitch rate (unitless). C_D, C_L, and C_m are unitless aerodynamic coefficients computed from look-up tables provided by NASA (Cunningham et al., 2008). The aerodynamic coefficients are provided in the airframe body axes, i.e. the raw data is provided for C_x, C_z, and C_m. This notation refers to standard aircraft body axis conventions (Stevens & Lewis, 1992). x is directed to the front along the longitudinal axis of the aircraft and z is directed down. X and Z represent the aerodynamic forces along the x and z axes, respectively. The body-axis look-up tables C_X and C_Z were transformed into lift and drag coordinates via a rotation of angle α about the lateral axis.

The GTM has two engines, one on the port side and the other on the starboard side of the airframe. Equal thrust settings for both engines is assumed. The thrust from a single engine T (N) is a function of the throttle setting δ_{th} (percent). $T(\delta_{th})$ is specified as a ninth-order polynomial in NASA's high fidelity GTM simulation model. T_x (N) and T_z (lbs) denote the projection of the total engine thrust along the body x-axis and body-z axis, respectively. T_m (N-m) denotes the pitching moment due to both engines. T_x, T_z and T_m

are given by:

$$T_x(\delta_{th}) = n_{ENG} T(\delta_{th}) \cos(\epsilon_2) \cos(\epsilon_3) \tag{13}$$

$$T_z(\delta_{th}) = n_{ENG} T(\delta_{th}) \sin(\epsilon_2) \cos(\epsilon_3) \tag{14}$$

$$T_m(\delta_{th}) = r_z T_x(\delta_{th}) - r_x T_z(\delta_{th}) \tag{15}$$

$n_{ENG} = 2$ is the number of engines. $\epsilon_2 = 1.98$ deg and $\epsilon_3 = 2.23$ deg are angles that specify the rotation from engine axes to the airplane body axes. $r_x = 0.128$ m and $r_z = 0.102$ m specify the moment arm of the thrust.

The elevator and throttle actuator dynamics are modeled as linear systems. These models presented in the Appendix.

3.2. Aircraft Trim and Model Linearization

A steady, level reference flight condition is chosen within the GTM flight envelope, around which a linear, time-invariant model of the vehicle is derived. The GTM is trimmed at the following condition:

$$\bar{\mathbf{x}} = \begin{bmatrix} V \\ \alpha \\ q \\ \theta \\ h \end{bmatrix} = \begin{bmatrix} 38.58 \text{ m/s} \\ 5.63 \text{ deg} \\ 0 \text{ deg/s} \\ 5.63 \text{ deg} \\ 152.4 \text{ m} \end{bmatrix}, \quad \bar{\mathbf{u}} = \begin{bmatrix} \delta_{th} \\ \delta_{elev} \end{bmatrix} = \begin{bmatrix} 33.098 \text{ \%} \\ 0.072 \text{ deg} \end{bmatrix} \tag{16}$$

The nonlinear GTM equations of motion are linearized about this trim condition to yield a 8-state system G with two inputs and five outputs. The additional three states are due to the inclusion of the aircraft actuators in the system. The associated state-space matrices are presented in the Appendix. This resulting linear model is used for control law development, initial filter synthesis, and simulation.

3.3. Control Law

Model-based fault detection approaches often use an open-loop model for detection algorithm design. This fails to account for closed-loop system behaviors which can be important to ascertain the capabilities of model-based techniques while operating on a closed-loop system (Pandita et al., 2011). Developing a simple control law serves that purpose.

The control law developed for this research is an altitude-hold, airspeed-hold autopilot with stability augmentation. The stability augmentation system is designed using H_∞ techniques and the pitch angle, airspeed, and altitude trackers are designed using classical PI control. The controller takes measurements of the five longitudinal aircraft states – velocity, angle-of-attack, pitch rate, pitch angle, altitude – and controls controls the elevator and throttle. Further details about controller design methodology and performance parameters are presented in (Freeman et al., 2011; Freeman, 2011), and the particular state-space matrices for the controller can be found in the Appendix of this paper.

3.4. Attitude Sensors

Sensors for angle of attack, pitch rate, and pitch angle are modeled as unity with additive white noise and bias on the true states. Equations 17-19 describe the state measurements used for control and fault detection; n_α, n_q, and n_θ represent the component of the respective measurement signal

occurring due to sensor noise.

$$\alpha_m = \alpha + n_\alpha \tag{17}$$

$$q_m = q + n_q \tag{18}$$

$$\theta_m = \theta + n_\theta \tag{19}$$

Attitude sensor dynamics are neglected in the NASA GTM and are similarly not considered in this paper to keep the attitude sensor modeling simple yet still capture the most significant noise effects. The attitude sensor noise parameters are derived from sensor data on the NASA GTM T2 aircraft and are presented in Table 3 (Cox, 2010). These noise levels are applied to

Table 3: Attitude sensor parameters

Noise Signal	**Standard Deviation**	**Bias**	**Scale Factor**
n_α	0.1031 deg	0.0 deg	1
n_q	0.14737 deg/s	-0.0115 deg/s	1
n_θ	0.105 deg	0.0 deg	1

signals in the nonlinear simulation. All FDI simulation results presented in this paper include sensor noise.

4. Fault Detection: H_∞-synthesis

The H_∞-synthesis framework is used to design filters to estimate disturbances, e.g. faults, at the plant input. H_∞ methods offer advantages over traditional Kalman filtering, including superior performance in the presence of model uncertainty and the ability to filter process noise and exogenous

disturbances without necessarily having a statistical model of those inputs (Simon, 2006).

4.1. H_∞ Problem Formulation

The H_∞ filtering problem is formulated as a variant of a standard H_∞ optimal control problem. For this application, the fault detection problem is formulated in the H_∞ filtering framework.

A H_∞ filter is synthesized based on the linearized GTM model described in Section 3.2 to estimate faults associated with the static and total pressure measurements. The effects of potential unmodeled dynamics are negelcted in this formulation. The closed-loop flight control system, including the

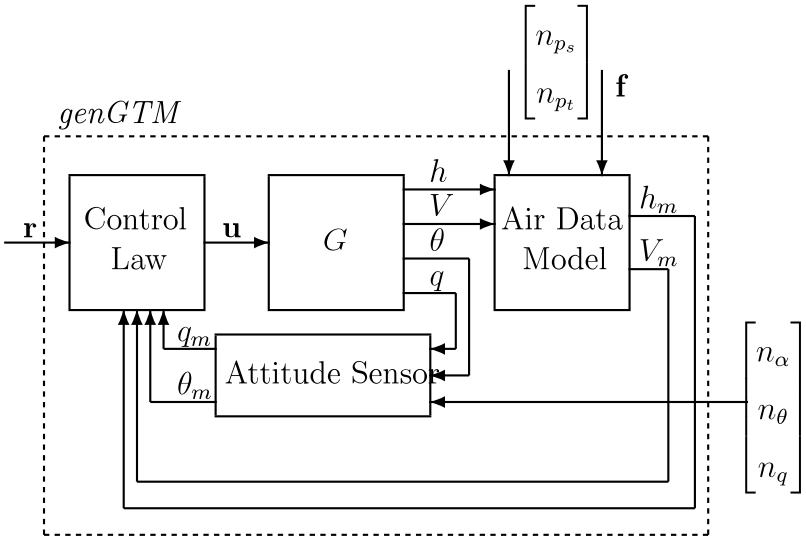

Figure 11: Interconnection for generalized plant *genGTM*

linearized aircraft dynamics, autopilot, attitude sensors and air data sen-

sors, is shown in Figure 11. The generalized plant, $genGTM$, has the following inputs: the autopilot reference signals $\tilde{\mathbf{r}} = \begin{bmatrix} V_{cmd} & h_{cmd} \end{bmatrix}^{\mathsf{T}}$, the attitude measurement noises, $\tilde{\mathbf{n}} = \begin{bmatrix} n_\alpha & n_q & n_\theta \end{bmatrix}^{\mathsf{T}}$, and the injected pitot faults $\tilde{\mathbf{f}} = \begin{bmatrix} f_{p_s} & f_{p_t} \end{bmatrix}^{\mathsf{T}}$. The errors $\tilde{\mathbf{e}}$ are the difference between the injected faults and estimated faults $\hat{\mathbf{f}} = \begin{bmatrix} \hat{f}_{p_s} & \hat{f}_{p_t} \end{bmatrix}^{\mathsf{T}}$.

Two different filter architectures are considered. In the first design, the generalized GTM plant measured outputs $\mathbf{y_I} = \begin{bmatrix} p_{s_m} & p_{t_m} & \alpha_m & q_m & \theta_m \end{bmatrix}^{\mathsf{T}}$ are made available to the fault detection filter. The second design utilizes control commands in addition to these measurements with the augmented filter input $\mathbf{y_{II}} = \begin{bmatrix} p_{s_m} & p_{t_m} & \alpha_m & q_m & \theta_m & \delta_{th} & \delta_{elev} \end{bmatrix}^{\mathsf{T}}$.

The air data fault models are included within the generalized GTM plant to generate faulted airspeed or altitude measurements. These faulted measurements result in an error between the autopilot reference command and the state measurements, and the error induces control action, affecting the unfaulted state measurements as well. The desired filter takes these measurements as inputs and correctly estimates the size of a fault affecting an air data sensor. This is accomplished using H_∞ filtering.

The objective of the H_∞ filter synthesis is to generate a stable filter F which minimizes norm between the disturbances and the errors. Because this formulation has a generalized plant that is already closed-loop, the filter can take advantage of the expected closed-loop system dynamics to generate fault estimates. These estimates are more accurate than estimates that would result from the common open-loop synthesis approach that does not model the dynamics associated with the expected operation of a controlled system in the field. Note that the pitot noise enters the system in the same manner

as pitot faults (see Figure 10). As a result, F tracks the sensor noise as well as the faults. Algorithms for processing the estimated fault information generated by F can compensate for this noise.

Weighting functions are used to describe the expected frequency content of the inputs and the desired frequency content of the errors, the normalized inputs $\begin{bmatrix} \mathbf{r} & \mathbf{n} & \mathbf{f} \end{bmatrix}^{\mathsf{T}}$ and outputs $\mathbf{e}$. Figure 12 shows the desired interconnection of the filter with the generalized plant $genGTM$ with signal weights and filter F. Input and output signals with tildes represent their respective normalized signals in physical units.

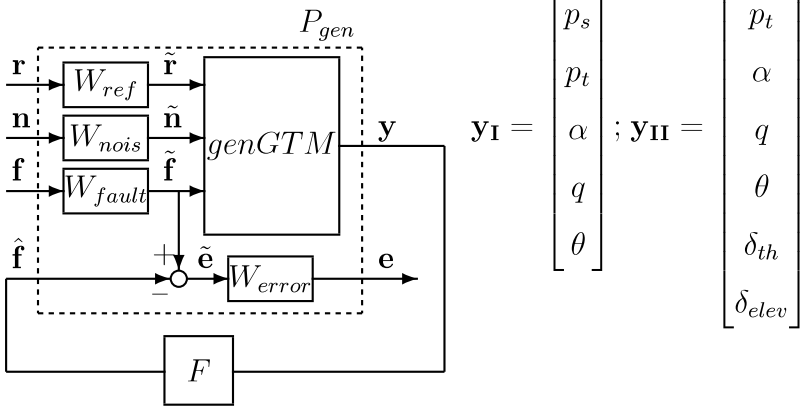

Figure 12: Interconnection for H_∞ filter synthesis

For fault detection, the disturbances are the autopilot reference signals $\mathbf{r}$ and the attitude measurement noises $\mathbf{n}$. The filter seeks to track the injected faults $\mathbf{f}$ with the fault estimates $\hat{\mathbf{f}}$ while rejecting attitude measurement noise $\mathbf{n}$ and reference commands $\mathbf{r}$. Similar H_2 and H_∞ model-matching approaches to FDI filter design have been applied in (Varga, 2003, 2009; Marcos et al., 2005; Ding, 2008a; Zolghadri et al., 2006; Mazarsand et al., 2008).

4.2. Signal Weighting Methodology

In signal-based H_∞ control design, the size of signals entering and exiting the system across frequencies are an important part of the optimization. Weighting functions can be used to describe the expected or known frequency content of exogenous signals. Additionally, the designer may desire error signals to have particular frequency content; weighting the error signals introduces those specifications into the problem formulation. Weights are also used for uncertainty modeling in order to reflect model accuracy across frequencies; system models are often more or less accurate in particular frequency ranges, and it is prudent to introduce uncertainty wherever the model dynamics are less accurate. For this application, weighting functions are initially applied to the exogenous inputs: reference commands, sensor noises, and faults. Additionally, the fault estimate errors are represented as performance weights.

Autopilot reference commands are expected to have little high-frequency content; thus, the most important consideration in choosing a reference command weighting function is normalizing the relative size of the altitude and input signals. This ensures that the weighted generalized plant properly reflects the relationship between the two reference command channels rather than reflecting a difference in units. A constant weighting function W_{ref} is used such that the H_∞-synthesis algorithm is not unduly sensitive to either reference command.

The weighting function W_{nois} represents the attitude sensor noise signals. Two considerations drive the selection W_{nois}. First, for mid-grade inertial sensors that may be utilized on a small UAV, the sensor noise magnitude is

often greater at high frequencies while the noise magnitude is reduced at low to intermediate frequencies. Second, the standard deviations of the noise in each channel of the inertial sensor measurements differ(Table 3). A dynamic weighting function is adopted, and the entries in W_{nois} are selected to reflect the differing measured noise levels in each sensor measurement as well as to embed information about expected sensor noise levels across frequency.

Next, W_{fault} represents the air data pressure fault inputs. The function is chosen such that the DC gain represents large faults (-20 dB). This value is selected based upon the aerospace industry standards and experimental data described in Sections 2.3-2.4. The weight is small for frequencies greater than 5 rad/s to penalize tracking of high frequency faults. The aircraft dynamics roll off near this frequency; hence, higher frequency faults do not manifest themselves within attitude sensor measurements. Finally, the error weighting function W_{error} represents the inverse of the allowable tracking error at each frequency. Normally, the error weight would be large at low frequency to ensure close tracking. Tracking at high frequency is less desirable and error weightings will roll off to some small high frequency gain. The particular nature of this problem, however, is such that the usual error weighting methodology cannot be adopted for the generalized GTM filter synthesis. Equation 20 shows the DC gain of $P_{\tilde{\mathbf{f}}\tilde{\mathbf{y}}}$, the partition of $genGTM$ from $\tilde{\mathbf{f}}$ to $\tilde{\mathbf{y}}$.

$$P_{\tilde{\mathbf{f}}\tilde{\mathbf{y}}}|_{\omega=0} = \begin{bmatrix} -0.0370 & 0.0370 \\ -0.0370 & 0.0370 \\ -49.984 & 49.984 \\ 0 & 0 \\ -49.984 & 49.984 \end{bmatrix} \tag{20}$$

Note that the matrix representing the DC gain is rank deficient. Thus, faults in the direction $\mathbf{f} = [1\ 1]^{\mathsf{T}}$ are indistinguishable from an unfaulted conditon. The unobservability of this fault direction at DC has a simple physical explanation. As shown by Equation 4, a simultaneous and equal fault in both pitot probes has no effect on the airspeed measurement. A fault in the $\mathbf{f} = [1\ 1]^{\mathsf{T}}$ direction only causes a bias in the altitude measurement. The model for the longitudinal dynamics is unaffected by a constant offset in altitude. Thus, a fault in the $\mathbf{f} = [1\ 1]^{\top}$ direction will cause the closed loop system to adjust to a biased value of altitude but all measurements will appear, in steady state, to converge back to their original trim conditions.

This rank deficiency places limits on the fault detection performance at low frequencies. For a filter F to ensure perfect fault tracking at low frequency, F must be a pseudoinverse of $P_{\tilde{\mathbf{f}}\tilde{\mathbf{y}}}$ over that frequency range. In particular, a filter F that would make the tracking error arbitarily small at low frequency cannot be synthesized by `hinfsyn` (Balas et al., 2010) because the partition is rank-deficient and its pseudoinverse does not exist.

To circumvent this problem, W_{error} is chosen such that the DC gain is small (-40 dB) and begins to roll up at very low frequency. For frequencies greater than 10^{-2}, the traditional approach of rolling off to a small

high frequency gain (-60 dB) is applied. This penalizes fault estimation performance at extremely low frequencies as well as high frequencies; such an architecture allows for improved filter performance at intermediate frequencies given the inherent system limitations. Additional detail regarding the weighting methodology and particular weights selected can be found in (Freeman, 2011).

4.3. FDI Filters

The weighted interconnection shown in Figure 12 is used to generate the weighted generalized plant P_{gen}. The filter F is synthesized with a H_∞-norm of 0.1045. Hence, the filter meets the desired objective encoded by the selected weighted functions. As described in Section 4.1, two filters with different architectures are synthesized. Filter F_I includes the air data measurements and attitude measurements as inputs. Filter F_{II} has an augmented input vector that also includes the control commands. The performance of the two filters will be analyzed and compared in the subsequent section.

5. H_∞ Fault Detection Results

This section examines the fault detection filters synthesized in Section 4 and assess fault detection performance for a variety of fault scenarios. The filters are integrated with the sensor models and GTM and are simulated while incorporating sensor noise and modeled input uncertainty.

5.1. Frequency Domain Comparison

The FDI filters F_I and F_{II} share five common inputs. The frequency responses from those common inputs to the fault estimates are quite similar

for the attitude measurement inputs. The frequency responses differ, however, from the pressure measurements to fault estimates. Figure 13 compares these magnitude responses for both filters. The five-input filter F_I has a sig-

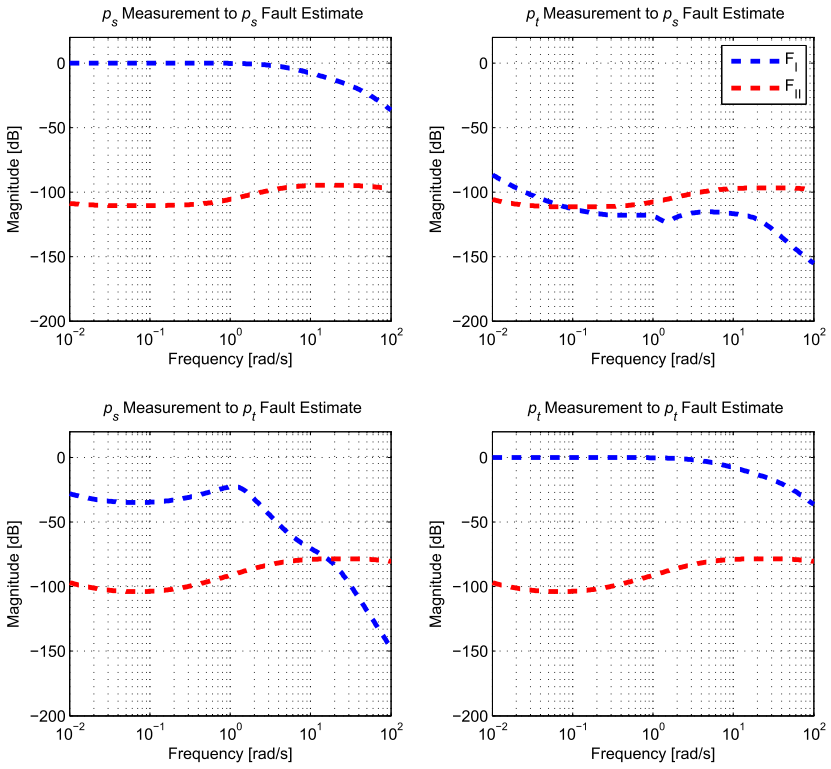

Figure 13: Bode Magnitude from pressure measurements to fault estimates

nificantly higher gain from the pressure measurements to the corresponding fault estimates than F_{II} exhibits. The nine-input filter is able to incorporate information about the autopilot reference commands and control positions to synthesize a fault estimate. The H_∞-synthesis algorithm led to the filter F_{II} relying less upon potentially corrupted pressure measurements to estimate their accuracy than F_I depends upon the pressure measurements. One can infer that pitot sensor noise will be more strongly attenuated by F_{II} than F_I,

and the resulting fault estimate signals can be expected to exhibit less noise effects.

5.2. Fault Detection Simulations

This subsection details the fault detection performance simulations conducted for a variety of fault modes. The first fault considered is a partial blockage of the static pressure port while the pitot inlet and drain hole remain unfaulted. This fault is modeled as a small step fault on the static pressure in the closed-loop nonlinear GTM model, based upon the industry standards and experimental results described in Sections 2.3-2.4. The total pressure measurement is unfaulted. Fault detection performance is also evaluated for a simulated drain hole blockage. This fault is modeled as an additive step on the total pressure in the nonlinear GTM models while the static pressure measurement remains unfaulted.

The performance of the synthesized filters are similarly examined for a simultaneous fault in p_s and p_t in the closed-loop nonlinear GTM. This represents a combination of the previous faults that may occur due to severe debris effects, ice accretion, or other causes. Finally, it is useful to understand the ability of the filter to detect time-varying faults. As described in Section 2, fouled airflow or liquid in the pneumatic lines can lead to time-varying pressure measurement errors. While these fault modes are not yet well-understood, analyzing performance for sinusoidal faults provides some insight to filter capabilities and limitations. The effects of high frequency content in the measurements are mitigated by the controller and the roll-off of the aircraft dynamics. Measurement frequency content that is slower than 1 rad/s, however, can induce significant control action. Two sinusoidal

faults in this frequency domain are injected and detection performance is compared.

A simple representation of certain air data blockages can be obtained by injecting step faults into the static and total pressure measurements. The performance of the synthesized filter under these scenarios is examined. The filter should yield estimates that track the generalized fault inputs reasonably quickly with minimal steady-state error. False positives are undesirable. Any fault detection system implemented with the goal of control reconfiguration must be sufficiently fast as to allow for reconfiguration before undesired aircraft maneuvers become unsafe.

Static Port Partial Blockage Detection

A simulation is conducted in which a step fault of magnitude 0.01 psi–representing a partially blocked static port–is injected into the static pressure measurement signal in the nonlinear GTM. Recall that the nonlinear GTM simulation includes the control algoritm, fault models, sensor noise, actuator uncertainty, and exogenous disturbances. This fault represents a partial blockage of a static port. Fault detection performance is examined using the both the measurements filter (F_I) and subsequently the augmented filter (F_{II}).

The simulation has a duration of 20 seconds and includes attitude and pitot sensor noise. For ideal detection performance, the fault estimate $\hat{\mathbf{f}}$ should track the fault signal $\mathbf{f}$ in the faulted static pressure channel (a *true positive* detection) and additionally indicate no fault in the unfaulted total pressure channel (a *true negative* detection).

At time $t = 1$ second, the blockage is initiated, and a comparison of

fault detection performance for both filters is shown in Figure 14. The

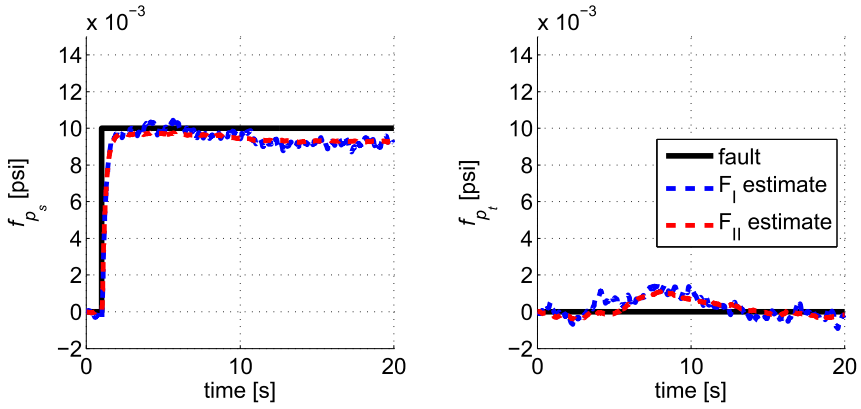

Figure 14: Fault estimation: p_s step fault, nonlinear GTM

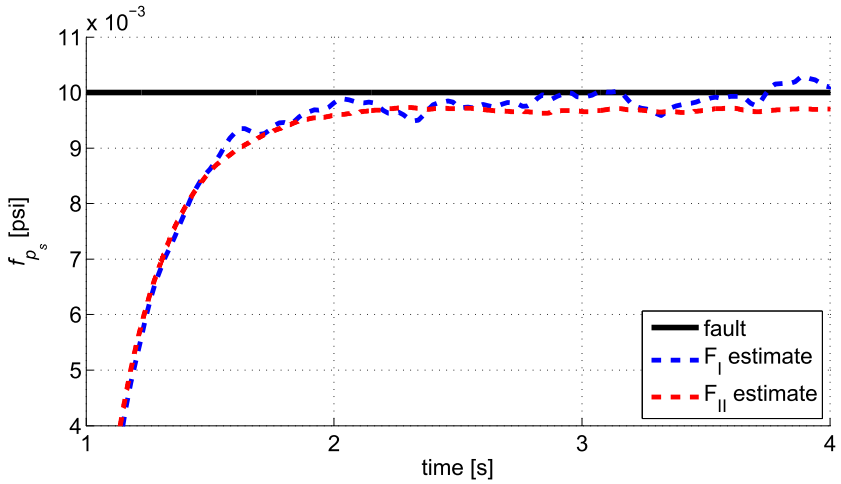

Figure 15: Fault estimation: short-term response of fault estimates to p_s step fault

filters detect the static pressure fault in the nonlinear model rapidly, rising to correctly estimate the fault magnitude within 1.5 seconds in the case of the original filter design. Figure 15 shows the fault estimate response in the seconds immediately ensuing the blockage. The fault estimates generated by

both filters rapidly rise and track the static pressure measurement fault with good accuracy in a short time frame.

Note that the estimates fluctuate throughout the simulation period. These fluctuations are the result of the GTM transient dynamic response to the static port blockage. Figure 16 shows the control action and longitudinal aircraft state responses throughout the simulation. It takes nearly a minute for the GTM to retrim about a new flight condition after the blockage fault is applied to the system. Over longer time periods, the filters will not yield errorless fault tracking due to the rank deficiency described in Section 4.2. The slowest filter pole has a frequency on the order of 10^{-5} rad/s, hence the fault estimation error will grow quite slowly. The fault estimate will eventually decay to zero in the faulted channel and drift away from zero in the unfaulted channel. Measures to combat this estimate drifting phenomenon must be designed into any algorithm that can be implemented on an operational system.

The fault estimates in both channels are noisy due to attitude and air data sensor noise. In these simulations, notice that the fault estimate in the total pressure fault channel will generally exhibit slightly higher noise levels relative to the static pressure fault estimate. As stated in Section 4.2, attitude sensor noise couples to the total pressure fault estimate more strongly than to the static pressure fault estimate. Hence, the filters rely on these measurements to detect the presence of a fault in the airspeed measurement more than it does for the altitude measurement. Since the attitude measurements are fed into the airspeed-hold autopilot, the total pressure fault estimate noise levels are larger. While the H_∞ filters are designed to minimize

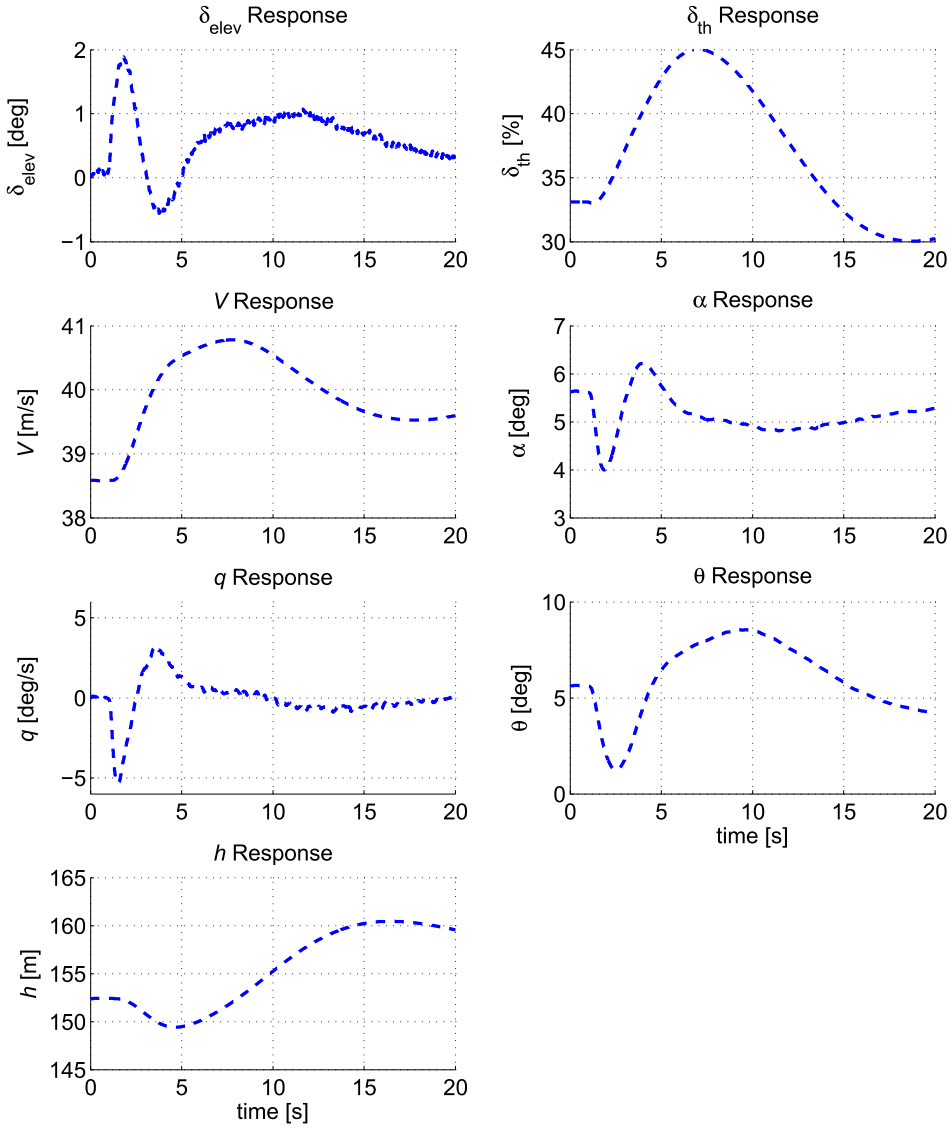

Figure 16: Aircraft state and control response: p_s step fault, nonlinear GTM

the effect of sensor noise on the fault estimates by penalizing high frequency filter outputs, noise in the estimates cannot be entirely eliminated. The augmented filter F_{II}, however, has a lower gain from its measurement inputs to fault estimates than F_I. With increased measurement signal attenuation, the resulting fault estimates exhibit lower noise levels.

Drain Hole Blockage Detection

The same simulations are conducted with a total pressure fault rather than a static pressure fault, representing the presence of a drain hole blockage. Figure 17 shows that the filters indicate a true positive detection in the total pressure channel with some residual noise for the reasons explained previously. Note that there is a larger error in the total pressure fault estimates in the presence of a drain hole blockage than for static pressure estimates in the presence of a static port blockage. This error diminishes as the GTM transient response dissipates. Additionally, both filters correctly indicate a true negative detection in the static pressure measurement channel.

Multiple Fault Detection

A more severe fault scenario is considered in this subsection. The two previous faults are modeled as occurring concurrently by simultaneously injecting a fault of equal magnitude injected into the static and total pressure channels. This scenario is unique because the faults will not change the airspeed measurement due to a constant dynamic pressure calculated by the air data system. A compound fault has limited effect on the air data measurements, hence it is interesting to examine the ability of the filters to detect such a condition. Again, 0.01 psi step faults are injected into both the static

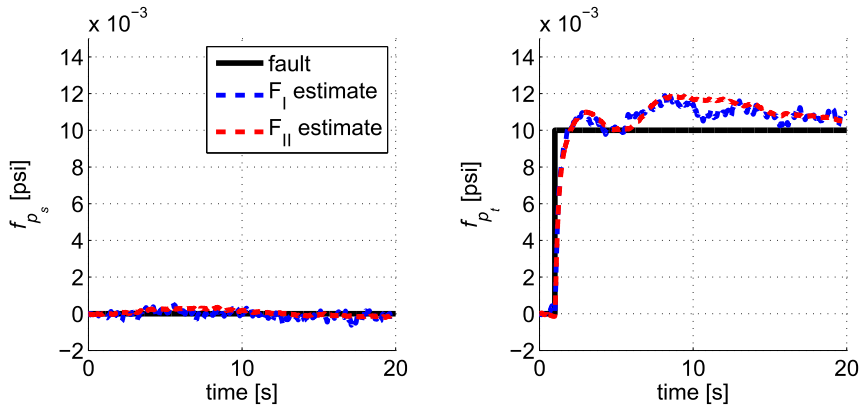

Figure 17: Fault estimation: p_t step, nonlinear GTM

and total pressure measurements at time $t = 1$ during a 20 second simulation.

Figure 18 shows the fault estimates for the simultaneous fault in the nonlinear GTM. The simultaneous fault results in a bias in the altitude measurement while the indicated airspeed is correct. In this fault scenario, all of the control inputs and aircraft states– except the altitude measurement–converge back to the original trim condition. The only effect of the simultaneous fault is that the aircraft converges to an offset altitude. Despite this limited manifestation of the fault in the state measurements, the filters achieve true positive detections in both pressure measurement channels. The filters use the attitude state measurements to track the fault by compensating for the dynamic response of the aircraft to the step changes in the measurements.

Time-Varying Fault Detection

It is possible that loose, partial port blockages or fluid in the pneumatic lines could cause time-varying fluctuations in the air data measurements.

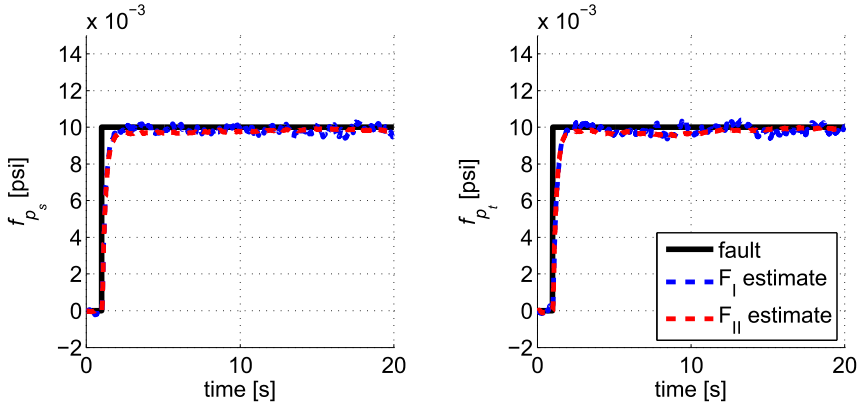

Figure 18: Fault estimation: simultaneous p_s and p_t step faults, nonlinear GTM

Therefore, a full analysis must include investigations into the ability of the fault detection algorithm to succeed in the event of a fault with frequency content.

High frequency variations in the pressure measurements do not adversely impact the GTM aircraft in controlled flight since the closed-loop aircraft dynamics roll off at moderate frequencies. Low-frequency fluctuations, however, could pose a problem as they are not attenuated.

Sinusoidal faults are introduced into the nonlinear GTM simulation to examine the ability of the filters to detect time-varying faults. The amplitude of the injected sinusoids is 0.01 psi – as with the step faults – and the first frequency considered is 0.03 radians per second. The faults are injected at $t = 0$ and run for 60 seconds in order to capture data over a larger fraction of the fault period. Figure 19 shows the fault estimate tracking for the nonlinear GTM model with a static pressure measurement fault. The filters track the slow sinusoidal fault well and properly indicate nominal operation for the unfaulted total pressure measurement channel. Hence, the results suggest

that a liquid blockage within an air data probe or fouled airflow could be detected if the time-varying effects of that fault are low frequency. The

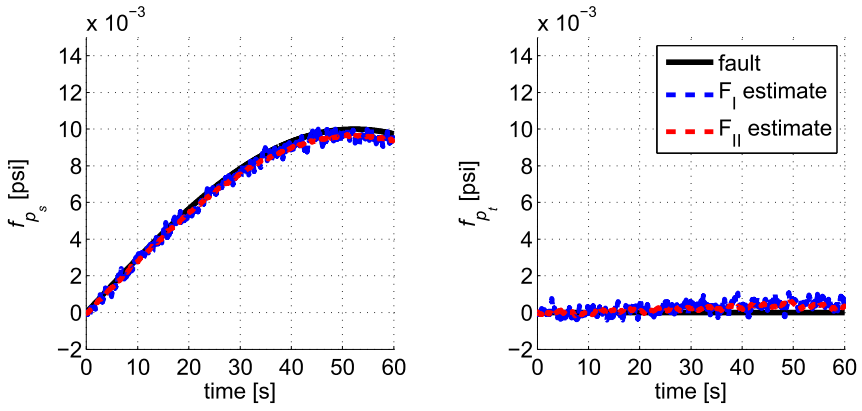

Figure 19: Fault estimation: p_s 0.03 rad/s sinusoidal fault, nonlinear GTM

filters have rapidly and accurately estimated injected steady-state faults and slowly time-varying faults, so detection capability of a higher frequency fault is considered. The previous simulation is run with a fault frequency of 0.3 radians per second – an order of magnitude faster – and all other parameters left the same. Figure 20 shows the fault estimates begin to drift away from the true fault.

With time, the estimates become sufficiently inaccurate to suggest a false positive fault identification in the total pressure channel. In this example, the augmented filter performance is comparable to the original filter performance throughout the duration of the fault. The performance degradation associated with this fault scenario can be understood by examining the aircraft control action and state history throughout the duration of the simulation, shown in Figure 21. This fault induces significant throttle control action, yielding large changes in attitude, airspeed, and altitude of the aircraft. As a

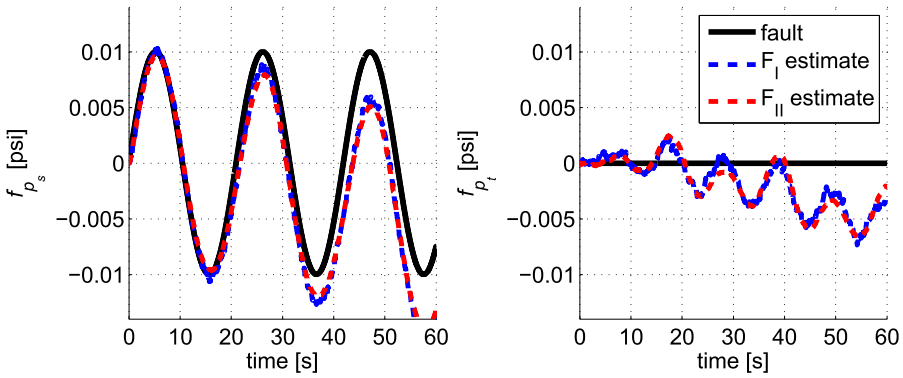

Figure 20: Fault estimation: p_s 0.3 rad/s sinusoidal fault, nonlinear GTM

result of this maneuvering, the aircraft is not operating at the flight condition for which the filters were designed, and fault detection performance suffers.

This example illustrates the degraded performance of the filter for time-varying faults of increasing frequencies. Moreover, it shows some limitations of a linear fault detection approach and filter design applied to a nonlinear system.

5.3. Summary

These experiments demonstrate that for partial static port blockages, drain hole blockages, and a combination of those faults modeled based on experimental air data results, the fault detection filters can rapidly yield true positive and true negative detections in a nonlinear simulation. Time-varying fault effects of fault modes such as airflow disruptions and liquid water blockages can also be characterized if the effects are of sufficiently low frequency. For all simulations, the most significant difference between the performance of F_I and F_{II} is that F_{II}–the filter which uses the aircraft sensor measurements, reference commands, and control positions–provides

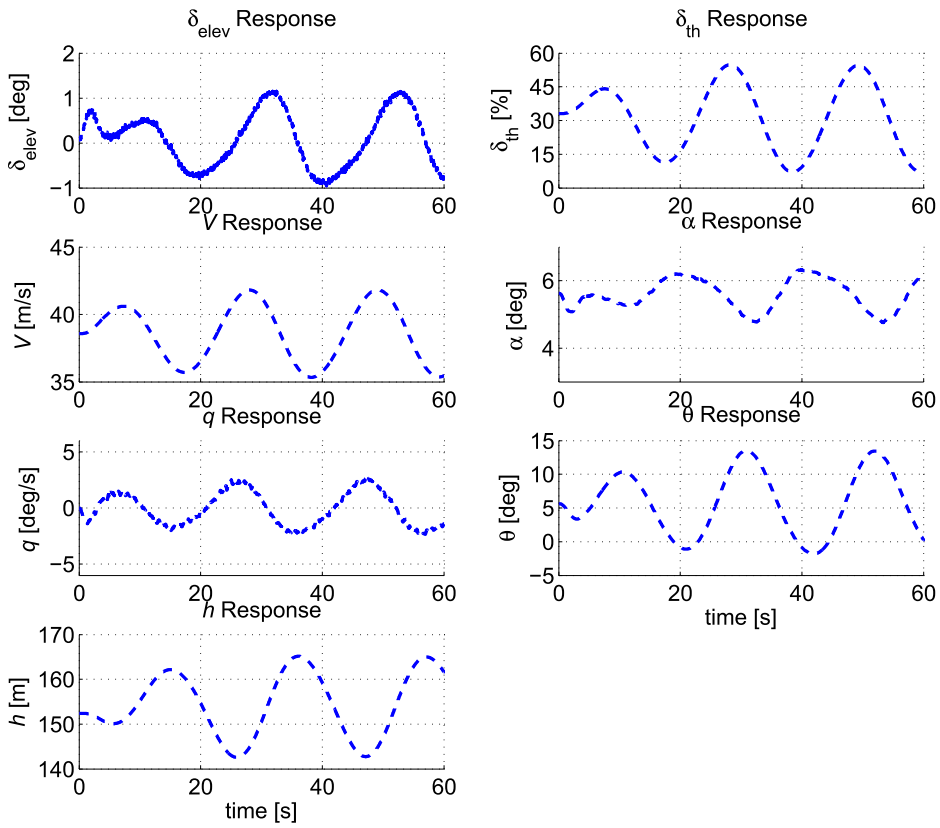

Figure 21: Aircraft state and control response: p_s sinusoidal fault, nonlinear GTM

slightly improved noise attenuation in its fault estimates. Overall speed and accuracy of response are comparable, indicating that supplying the filter with additional information does not yield significant performance gains.

6. Conclusion

This paper developed a low order model of an air data system and blockage faults based upon first-principles knowledge of industry-standard devices and experimental results. Simple faults were emphasized, but faults involving more complex heating mechanisms and slow-acting sensor drift pose difficult

challenges for air data system reliability. In order to provide true fault tolerance for air data systems, Further enhancements to air data probe modeling must be made in order to better detect and identify sensor faults.

Modeling of blockage faults, however, has enabled a model-based fault tolerance approach that has yielded significant results. Models of blocked air data probes were integrated with the nonlinear longitudinal model of the NASA GTM aircraft in order to provide a fault detection research platform. Using this platform, this paper detailed a method to detect faults using H_∞ robust filters. Two filter architectures were considered, and their fault detection performance was first compared in simulations of the GTM aircraft affected by the following fault modes: static port blockage, drain hole blockage, and a combined static port and drain hole blockage. In each case, both filter architectures rapidly detected the presence of a fault and accurately estimated the fault magnitude. Next, time-varying fault effects of fault modes such as airflow disruptions and liquid water blockages were simulated with the GTM. For sufficiently low-frequency faults, the filters yielded estimates that accurately characterized the faults. Higher frequency faults were not estimated as accurately and resulted in significant false positive detection by both filters. Such faults induced significant aircraft maneuvering away from the trim condition for which the filters were designed. This indicates the necessity for improving detection capabilities for time-varying air data faults that are slower than the aircraft bandwidth and that induce significant control action.

Another important goal is to enhance the fault detection algorithms so that estimates are more accurate at flight conditions other than the con-

dition for which the filter was designed. This paper has considered fault detection performance for small maneuvers over a small segment of the flight envelope. Extending these results to a broad flight envelope is an important next step. At these 'off-design' conditions, FDI filters should maintain their responsiveness and accuracy in order to achieve significant improvements in fault-tolerance.

Acknowledgements

This work received financial and technical support from Goodrich Sensors and Integrated Systems. Their knowledge of industry-leading air data systems and access to their experimental facilities was integral to this research. Thanks to Bill Kunik, Brian Mathies, Tim Golly, and others who assisted in this effort. Additionally, this material is based upon work supported by the National Science Foundation under Grant No. 0931931 entitled CPS: Embedded Fault Detection for Low-Cost, Safety-Critical Systems. Any opinions, findings, and conclusions or recommendations expressed in this material are those of the author and do not necessarily reflect the views of the National Science Foundation.

References

References

ACC News Service (2008). B-2 accident report released. *http://www.af.mil/news/story.asp?id=123101727*, .

Balas, G., Chiang, R., Packard, A., & Safonov, M. (2010). *Robust Control Toolbox*. The MathWorks.

Bleeg, R. (1988). Commercial jet transport fly-by-wire architecture considerations. In *AIAA/IEEE Digital Avionics Systems Conference* (pp. pp. 399–406).

Bureau d'Enquêtes et d'Analyses (2011). Accident to the airbus a330-203 flight af 447 on 1st june 2009: Update on investigation.

Collinson, R. (2003). *Introduction to Avionics Systems*. (2nd ed.). Kluwer.

Cox, D. (2010). *The GTM DesignSim v1006*.

Cunningham, K., Foster, J. V., Murch, A. M., & Morelli, E. (2008). Practical application of a subscale transport aircraft for flight research in control upset and failure conditions. In *AIAA Guidance, Navigation, and Control Conference, Honolulu, Hawaii*.

Ding, S. X. (2008a). *Model-based Fault Diagnosis Techniques*. Springer.

Ding, S. X. (2008b). *Model-based Fault Diagnosis Techniques: Design Schemes, Algorithms, and Tools*. (1st ed.). Springer.

Federal Aviation Administration (2009). *Advisory Circular 91-85 (Authorization of Aircraft and Operators for Flight in Reduced Vertical Separation Minimum Airspace)*. U.S. Department of Transportation.

Freeman, P. (2011). *Robust fault detection for commercial transport air data probes*. Master's thesis University of Minnesota.

Freeman, P., Seiler, P., & Balas, G. (2011). Robust fault detection for commercial transport air data probes. In *IFAC 18th World Congress*.

Gertler, J. J. (1998). *Fault detection and diagnosis in engineering systems*. (1st ed.). Marcel Dekker.

Goodrich (2002). *Air Data Handbook*. Goodrich Corportation – Sensors and Integrated Systems.

Isermann, R. (2005). *Fault-diagnosis systems: an introduction from fault detection to fault tolerance*. (1st ed.). Springer.

Marcos, A., Ganguli, S., & Balas, G. (2005). An application of H_∞ fault detection and isolation to a transport aircraft. *Control Engineering Practice*, *Vol. 13*, pp. 105–119.

Mazarsand, E., Jaimoukha, I., & Li, Z. (2008). Computation of a reference model for robust fault detection and isolation residual generation. *Journal of Control Science and Engineering*, (pp. pp. 1–12).

Murch, A., & Foster, J. (2007). Recent NASA research on aerodynamic modeling of post-stall and spin dynamics of large transport airplanes. In *45th AIAA Aerospace Sciences Meeting and Exhibit, Reno, Nevada* AIAA-2007-463.

Pandita, R., Bokor, J., & Balas, G. (2011). Closed-loop performance metrics for fault detection and isolation filter and controller interaction. *International Journal of Robust and Nonlinear Control*, .

Simon, D. (2006). *Optimal State Estimation: Kalman, H_∞, and Nonlinear Approaches*. John Wiley & Sons.

Stevens, B., & Lewis, F. (1992). *Aircraft Control and Simulaion*. John Wiley & Sons.

Varga, A. (2003). On computing least order fault detectors using rational nullspace bases. In *In Proceedings of the IFAC Symp. SAFEPROCESS'2003, Washington D.C.*.

Varga, A. (2009). General computational approach for optimal fault detection. In *SAFEPROCESS '09, Barcelona, Spain*.

Yeh, Y. (1996). Triple-triple redundant 777 primary flight computer. In *Proceedings of the 1996 IEEE Aerospace Applications Conference* (pp. pp. 293–307).

Yeh, Y. (1998). Design considerations in Boeing 777 fly-by-wire computers. In *Third IEEE International High-Assurance Systems Engineering Symposium* (pp. pp. 64–72).

Zolghadri, A., Castang, F., & Henry, D. (2006). Design of robust fault detection filters for multivariable feedback systems. *International journal of modelling and simulation, ACTA Press, Vol. 26*.

Appendix A. Design Data

This appendix provides the actuator models, linear GTM models, and controller models used for filter design and simulation described in this paper.

Appendix A.1. Actuator Models

The actuator dynamics are modeled as linear systems. The elevator actuator, Act_{elev}, for the longitudinal GTM is a 5Hz bandwidth, first-order sys-

tem with a 10 ms delay and is shown in Equation A.1. The engine dynamics, Act_{th}, are modeled as the second order system shown in Equation A.2.

$$Act_{elev} = e^{-0.01s}\frac{31.42}{s+31.42} \tag{A.1}$$

$$Act_{th} = \frac{-0.147s+0.731}{s^2+1.36s+0.731} \tag{A.2}$$

Appendix A.2. GTM State-space Matrices

The nonlinear GTM dynamics are linearized about the trim condition specified in Equation 16, yielding the two input, five output, and eight state system shown in Equation A.3.

$$\begin{aligned}\dot{\mathbf{x}} &= A_g\mathbf{x} + B_g\mathbf{u}\\ \mathbf{y} &= C_g\mathbf{x} + D_g\mathbf{u}\end{aligned} \tag{A.3}$$

The state-space matrices used in this model are presented in Equations A.4-A.7.

$$A_g = \begin{bmatrix} -0.072 & -0.150 & 0.002 & -0.332 & 0 & -0.012 & 0.063 & -0.200 \\ -0.384 & -2.367 & 0.942 & 0.000 & 0 & 0.001 & -0.003 & -1.865 \\ -0.862 & -39.443 & -3.285 & 0 & 0 & -0.153 & 0.757 & -310.207 \\ 0 & 0 & 1.0000 & 0 & 0 & 0 & 0 & 0 \\ 0 & -1.309 & 0 & 1.309 & 0 & 0 & 0 & 0 \\ 0 & 0 & 0 & 0 & 0 & 1.336 & -0.731 & 0 \\ 0 & 0 & 0 & 0 & 0 & 1.000 & 0 & 0 \\ 0 & 0 & 0 & 0 & 0 & 0 & 0 & -31.416 \end{bmatrix} \tag{A.4}$$

$$B_g = \begin{bmatrix} 0 & 0 \\ 0 & 0 \\ 0 & 0 \\ 0 & 0 \\ 0 & 0 \\ 1 & 0 \\ 0 & 0 \\ 0 & 4 \end{bmatrix} \tag{A.5}$$

$$C_g = \begin{bmatrix} I_5 & 0_{5\times 3} \end{bmatrix} \tag{A.6}$$

$$D_g = \begin{bmatrix} 0_{5\times 2} \end{bmatrix} \tag{A.7}$$

This resulting linear model is used for control law development, initial filter synthesis, and simulation.

Appendix A.3. Control Law State-Space Matrices

The altitude-hold and airspeed-hold autopilots with stability augmentation can be represented by the single state-space model with seven inputs, two outputs, and nine states:

$$\begin{aligned} \dot{\mathbf{x}}_\mathbf{c} &= A_c\mathbf{x}_\mathbf{c} + B_c\mathbf{u} \\ \mathbf{y} &= C_c\mathbf{x}_\mathbf{c} + D_c\mathbf{u} \end{aligned} \tag{A.8}$$

where $\mathbf{x_c}$ is the vector of controller states, $\mathbf{u}$ is the vector of inputs to the controller (composed of autopilot reference commands and aircraft state measurements), and $\mathbf{y}$ is the controller output (actuator commands). The state-

space matrices for the controller are shown in Equations A.9-A.16.

$$A_c = \begin{bmatrix} A_{c_{1,1}} & 0_{7\times 2} \\ 0_{2\times 7} & A_{c_{2,2}} \end{bmatrix} \tag{A.9}$$

$$A_{c_{1,1}} = \begin{bmatrix} -20.172 & 21.172 & -21.172 & 21.172 & -10.586 & -0.700 & 0.348 \\ 28.918 & -29.918 & 30.918 & -30.918 & 15.459 & 0.894 & -0.445 \\ -7.923 & 7.923 & -8.923 & 9.923 & -4.961 & 0.203 & -0.101 \\ -6.007 & 6.007 & -6.007 & 5.007 & -2.003 & -0.850 & 0.423 \\ 6.279 & -6.279 & 6.279 & -6.279 & 2.139 & 0.761 & -0.379 \\ 0 & 0 & 0 & 0 & 0 & 0 & -0.600 \\ 0 & 0 & 0 & 0 & 0 & 0 & 0 \end{bmatrix} \tag{A.10}$$

$$A_{c_{2,2}} = \begin{bmatrix} -18.925 & -7.462 \\ 8.000 & 0 \end{bmatrix} \tag{A.11}$$

$$B_c = \begin{bmatrix} 0.837 & 0 & -0.837 & 0 & 0.304 & 0.581 & 0 \\ -1.069 & 0 & 1.069 & 0 & -0.293 & -0.742 & 0 \\ -0.243 & 0 & 0.243 & 0 & 0.073 & -0.169 & 0 \\ 1.016 & 0 & -1.016 & 0 & 0.053 & 0.706 & 0 \\ -0.910 & 0 & 0.910 & 0 & -0.032 & -0.632 & 0 \\ -1.440 & 0 & 1.440 & 0 & 0 & -1.000 & 0 \\ 0.500 & 0 & -0.500 & 0 & 0 & 0 & 0 \\ 0 & 4.000 & 0 & 0 & 0 & 0 & -4.000 \\ 0 & 0 & 0 & 0 & 0 & 0 & 0 \end{bmatrix} \tag{A.12}$$

$$C_c = \begin{bmatrix} 0_{1\times 7} & C_{c_{1,2}} \\ C_{c_{2,1}} & 0_{1\times 2} \end{bmatrix} \tag{A.13}$$

$$C_{c_{1,2}} = \begin{bmatrix} 1.313 & 0.820 \end{bmatrix} \tag{A.14}$$

$$C_{c_{2,1}} = \begin{bmatrix} 14.971 & -14.971 & 14.971 & -14.971 & 7.485 & 0.011 & -0.005 \end{bmatrix} \tag{A.15}$$

$$D_c = \begin{bmatrix} 0 & 0 & 0 & 0 & 0 & 0 & 0 \\ -0.013 & 0 & 0.013 & 0 & -0.035 & -0.009 & 0 \end{bmatrix} \tag{A.16}$$

Integrating these models with the linear aircraft sensor models described in Section 2 constitutes the complete linear GTM model used in this research.